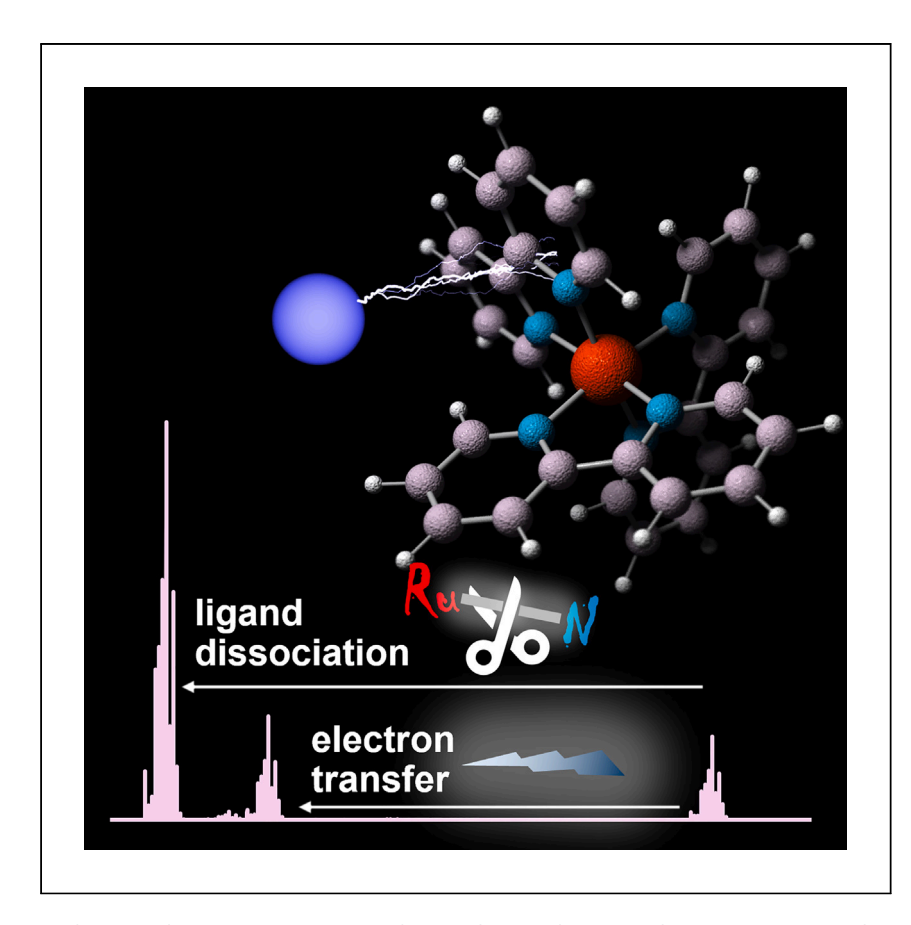


Article

Ruthenium diimine ion pairs exhibit diverse intra- and intermolecular dynamics



Ruthenium diimines are common photoredox catalysts, yet their interactions with anions are not well understood. Here, Schilter et al. describe the gas-phase chemistry of ion pairs featuring dicationic complexes and common monoanions, finding that the ion pairs are conformationally dynamic and more reactive than is commonly believed.

David Schilter, Umberto Terranova, Rebecca R. Robinson

schilter@txstate.edu

Highlights

Mass spectrometry of [Ru(diimine)₃]²⁺/X⁻ ion pairs reveals diverse fragmentation

Diimine ligands dissociate or undergo hydride attack, reduction, or deprotonation

Ion mobility spectrometry of ion pairs shows their sizes to follow the anion sizes

Ion pairs of non-basic anions are particularly dynamic on the picosecond timescale

Schilter et al., Cell Reports Physical Science 5, 102071

July 17, 2024 © 2024 The Author(s). Published by Elsevier Inc.

https://doi.org/10.1016/j.xcrp.2024.102071





Article

Ruthenium diimine ion pairs exhibit diverse intra- and intermolecular dynamics

David Schilter, 1,4,* Umberto Terranova, 2 and Rebecca R. Robinson 1,3

SUMMARY

The chemistry of cationic complexes depends on attendant anions, yet we know little about ion pairing. Here, we use mass spectrometry to study intra-cation and cation-anion interactions between ruthenium diimines $[Ru(bipy)_3]^{2+}$ (bipy = 2,2'-bipyridine), $[Ru(phen)_3]^{2+}$ (phen = 1,10-phenanthroline), and $[Ru(bipy)_2(phen)]^{2+}$ and $X^- = F^-$, Cl^{-} , Br^{-} , l^{-} , PF_{6}^{-} , HCO_{2}^{-} , AcO^{-} , BPh_{4}^{-} , and BAr_{4}^{F} (Ar^{F} = 3,5-bis(trifluoromethyl)phenyl). Ion pairs {[Ru(bipy)₃]X}⁺ undergo ionic bond cleavage to give [Ru(bipy)₃]²⁺ or experience bipy loss or fracture. X can effect hydride or electron transfer or deprotonation to afford $[Ru(bipy)_2(bipyH)]^+$, $[Ru(bipy)_2(bipy \cdot)]^+$, and $[Ru(bipy)_2(bipy-H)]^+$, respectively. Electron transfer and deprotonation correlate with anion redox potentials and proton affinities, respectively. Ion mobility spectrometry and density functional theory suggest that halides bind between diimines, while large anions protrude. Ion pair sizes follow radii of gyration predicted by molecular dynamics, which show ion pairs of non-basic anions to be especially fluxional. Our methods offer detailed information on inner- and outer-coordination spheres.

INTRODUCTION

Molecular photocatalysis research often exploits highly absorbent sensitizers that are, save for electron transfer reactions, chemically inert. Archetypal among sensitizers are ruthenium diimines, whose excited states are good oxidants and reductants. ^{1,2} In the case of $[Ru(bipy)_3]^{2+}$ (bipy = 2,2'-bipyridine; Figure 1A), the photoexcited species $[Ru(bipy)_3]^{2+*}$ undergoes oxidative or reductive quenching to respectively afford $[Ru(bipy)_3]^{3+}$ or $[Ru(bipy)_3]^{+}$. These radicals then either operate on a substrate or engage in electron transfer with a metal redox catalyst. For example, $[Ru(bipy)_3]^{+}$ derived from reductive quenching can reduce a co-catalyst as part of the hydrogen evolution reaction (Figure 1B).²

Ruthenium diimines have found success because the strong splitting of their 4d orbitals favors metal-to-ligand charge transfer³ and confers structural stability during catalysis, despite electronic excitation and redox. Yet, years before the present "renaissance" in molecular photocatalysis came reports describing the reactivity of bipy derivatives bound to ruthenium. For example, the monocation $[Ru(bipy)_3]^+$ is a good reductant in aqueous solution but can also add alkyl radicals $R \cdot$ to give $[Ru(bipy)_2(bipyR)]^+$, which feature dearomatized anionic ligands $[bipyR]^{-}$. Conversely, trication $[Ru(bipy)_3]^{3+}$ may oxidize a catalyst or substrate but can be susceptible to nucleophilic addition, for example by HO⁻ to give $[Ru(bipy)_2(bipyOH)]^{2+}$, in which anionic $[bipyOH]^-$ has a hydroxyl at a C6 atom. 6,7



¹Department of Chemistry and Biochemistry, Texas State University, San Marcos, TX 78666,

²Faculty of Medicine and Health Sciences, The University of Buckingham, MK18 1EG Buckingham, UK

³Department of Chemistry and Physics, Western Carolina University, Cullowhee, NC 28723, USA

⁴Lead contact

^{*}Correspondence: schilter@txstate.edu https://doi.org/10.1016/j.xcrp.2024.102071



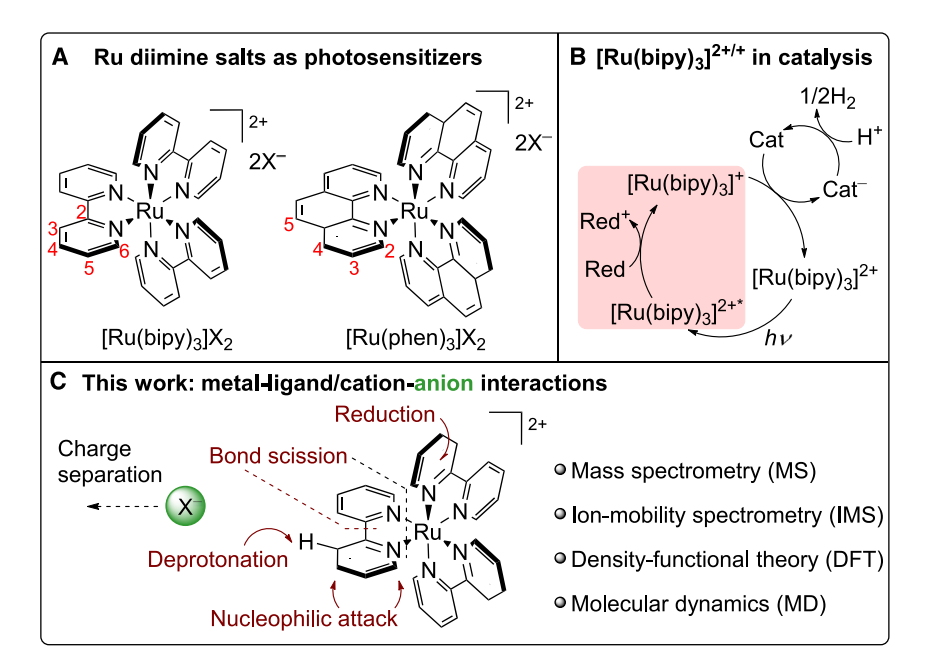


Figure 1. Ruthenium diimines are common photosensitizers

- (A) The atom numbering in bipy and phen complexes.
- (B) Reductive quenching (pink shading) of dications affords monocations, which are key intermediates in catalytic reductions.
- (C) This paper describes the covalent interactions within dications $[Ru(N^{N})_{3}]^{2^{+}}$ and their non-covalent interactions with anions. We learn of ion pairs' stability and dissociation (MS), sizes (IMS), structures (DFT), and dynamics (IMS).

Ruthenium diimines follow multiple photochemical⁸ and thermal reaction channels, both of which afford complex mixtures that can be made tractable using mass spectrometry (MS). In terms of thermal reactions, early work on $[M(bipy)_3]X_2$ (M = Fe, Ru; $X^- = Cl^-$, ClO_4^- , PF_6^-) showed it to give $[M(bipy)_3]^{2+}$ as well as many fragment ions.^{9,10} Indeed, ionization of $[M(bipy)_3]Cl_2$ salts and collision-induced dissociation (CID) caused loss of bipy to afford $[M(bipy)_nCl]^+$ (n=1,2). Similarly, $[M(bipy)_3](ClO_4)_2$ gave $[M(bipy)_2O_2]^+$, while $[M(bipy)_3](PF_6)_2$ gave $[M(bipy)_nF]^+$ (n=1,2)—products of anion abstraction from ClO_4^- and PF_6^- .

We are motivated to study ion pairs because the nature of anions—even those deemed "non-coordinating"—can greatly affect the chemistry of complex cations, not least those that star in thermal and photoredox catalysis. For example, derivatives of the salt $[Ir(ppy)_2(bipy)]X$ (ppy = (2-phenyl)pyridyl anion) in 1,4-dioxane exist as contact ion pairs when $X^- = PF_6^-$ but solvent-separated ion pairs when $X^- =$ $BAr_4^{F_4}$ (Ar = 3,5-bis(trifluoromethyl)phenyl). The latter are more amenable to reductive guenching than the former, which prompted us to ask more general and fundamental questions. How do subtle differences in anions affect the chemistry of ion pairs? How do the basicity and reducing power of X⁻ change their chemistry with cationic complexes? Here, we answer these questions in the gas phase by measuring mass spectra of charged ion pairs like {[Ru(bipy)₃]X}+ (Figure 1C), {[Ru(phen)₃ $[X]^+$, and $[[Ru(bipy)_2(phen)]X]^+$ (phen = 1,10-phenanthroline). These each feature complex dications and outer-sphere X⁻ monoanions, and we show how these exhibit diverse binding and dissociation channels, many of which give topical chargereduction products featuring modified diimines. Briefly, we measure MS of [Ru(bipy)₃]²⁺/2X⁻ mixtures and mass-select the charge-reduction products and ions pairs for further study by CID through MS/MS (Figure S1). The mass-selected

Article



ion pairs $\{[Ru(N^N)_3]X\}^+$ $(N^N = bipy, phen)$ we also study by ion mobility spectrometry (IMS) to learn about the relative sizes of these non-covalent assemblies. ¹² Lastly, we complement our experiments with static calculations and molecular dynamics (MD), both based on density functional theory (DFT), to support structural assignments and learn about the strengths and structural variability of cation-anion interactions. Collectively, these methods let us probe the inner- and outer-coordination spheres of our complex ions.

RESULTS AND DISCUSSION

Mass spectrometry

We first describe positive-ion electrospray ionization (ESI) MS of $[Ru(bipy)_3]Cl_2$, $[Ru(phen)_3]Cl_2$, and $[Ru(bipy)_2(phen)]Cl_2$. We treated the racemic chloride salts with two molar equivalents of tetra(n-butyl)ammonium salts nBu_4NX ($X^- = F^-$, Br^- , I^- , PF_6^- , AcO^-) or sodium salts NaX ($X^- = HCO_2^-$, BPh_4^- , BAr_4^F) to give dilute MeOH solutions for ESI-MS. We selected anions X^- that (1) span the gamut of coordinating/basic to "non-coordinating" and/or (2) are popular in photoredox catalysis or solar cells. Fully annotated high-resolution spectra for each complex-anion combination (Figures S2–S96), as well as a list of all ions observed (Table S1), are in the supplemental information. Increasing the capillary voltage effects increasingly energetic in-source fragmentation with N_2 gas. Thus, we go from having intact ion pairs ($[Ru(N^N)_3]X^+$ (green species in Figure 2A) and dications $[Ru(N^N)_3]^{2+}$ (blue) as the predominant Ru-containing ions to seeing fragments such as $[Ru(N^N)_2X]^+$ (black), which form when coordinating anions such as halides and carboxylates in the outer sphere replace N^N , forming a new Ru-X bond and lowering the charge of the complex.

In addition to anion and diimine loss, ion pairs also undergo ligand-centered reactions (maroon). For example, basic anions promote "rollover" ruthenation at a C3 site of bipy to give $[Ru(bipy)_n(bipy-H)]^+$ (n=1,2), complexes of the anionic N,C-donor $[bipy-H]^-$ (Figure 2B). Rollover, which is so named because one ring in a biaryl rotates 180° about the central C–C bond, 13,14 is the reason why base-catalyzed deuteration of $[Ru(bipy)_3]^{2+}$ exclusively affords $[Ru(bipy-3,3'-d_2)_3]^{2+}$. In contrast, $[Ru(phen)_3]^{2+}$ is inert toward deuteration because phen has less steric strain and flexibility than does bipy. Thus, it is curious that we see deprotonation of $[Ru(phen)_3]^{2+}$ despite the impossibility of rollover, a prospect that we describe in later sections.

Aside from deprotonation, other ligand-centered reactions involve diimines being attacked by H $^-$ and Me $^-$, which are decarboxylation products of HCO $_2$ $^-$ and AcO $^-$, respectively. We also see phen methylation in the absence of AcO $^-$, possibly due to reactions with MeOH solvent. Decarboxylation is common in MS, 16 and examples include conversion of group 10 acetates [M(phen)OAc] $^+$ (M = Ni, Pd, Pt) into the respective methyls 17 and CO $_2$ extrusion from formate [Ag $_2$ (Ph $_2$ P(CH $_2$) PPh $_2$)(O $_2$ CH)] $^+$ to give a hydride. 18 Our results are distinct because HCO $_2$ $^-$ and AcO $^-$ are counteranions rather than inner-sphere ligands, so H $^-$ and Me $^-$ attack ligands rather than the metal.

Lastly, the low electronegativity of I sees I⁻ reduce $[Ru(bipy)_3]^{2+}$ to the radical monocation $[Ru(bipy)_3]^+$, for which the consensus description $[Ru^{II}(bipy)_2(bipy \cdot)]^+$ is favored over the $[Ru^{II}(bipy)_3]^+$ alternative. This electron transfer mirrors the chemistry in Ru-sensitized solar cells that feature I⁻/I₃⁻ redox mediators. This redox reaction and the aforementioned ligand-centered reactions are "charge-reduction" processes that reflect how a system avoids charge-separation, which is very



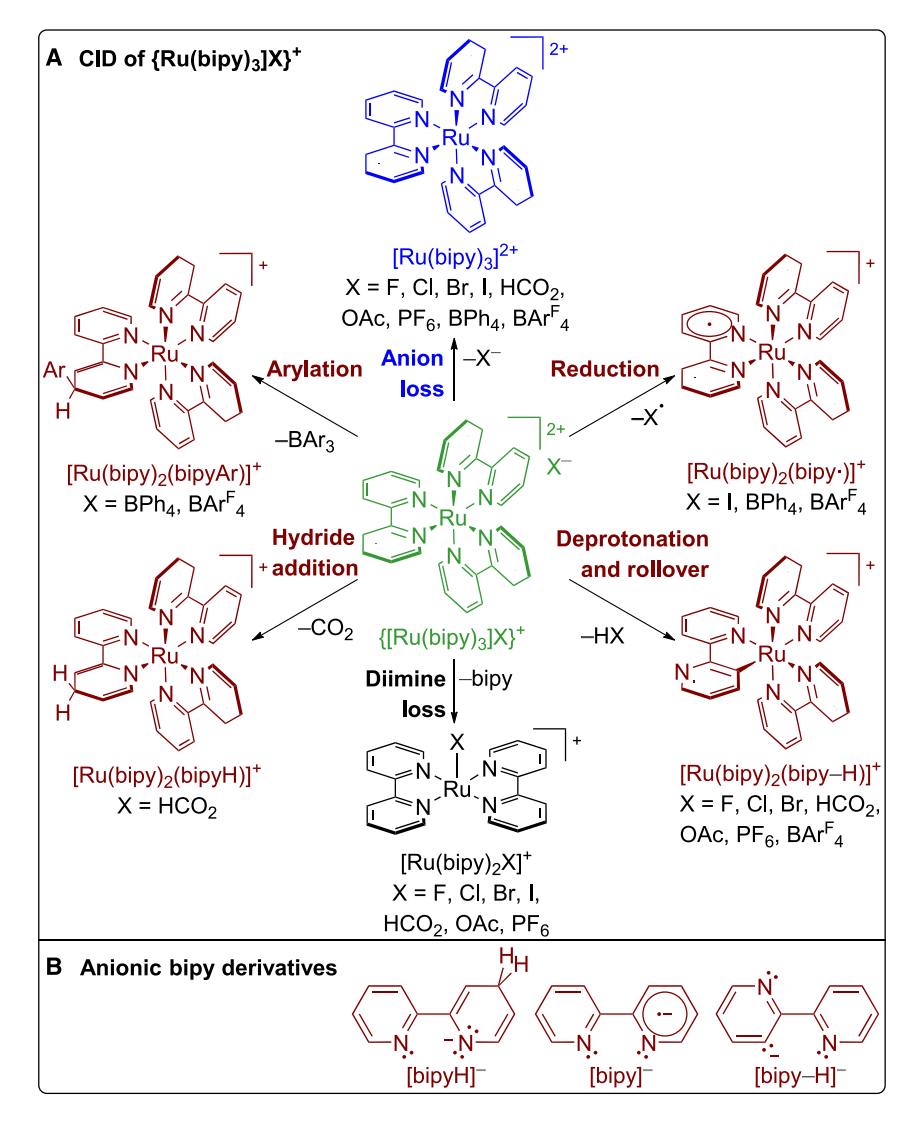


Figure 2. The products of {[Ru(bipy)₃]X}⁺ CID depend on the identity of anion X

(A) CID affords diverse products/processes: ion pairs (green), diimine dissociation products (black), ligand-centered reactions (maroon), and dications (blue).

(B) Coordinated ligands are often converted into anionic derivatives, examples of which are pictured here in the case of bipy.

unfavorable in the gas phase because Coulombic forces are $\sim 80\,\text{x}$ stronger in a vacuum than they are in liquid H_2O , a strong dielectric. 21,22 Thus, the strong interactions that charge-dense dications such as $[Ru(N^{\wedge}N)_3]^{2^+}$ have with anions in the gas phase mean that collisionally separating $[Ru(N^{\wedge}N)_3]^{2^+}$ from X^- often leads to charge reduction—deprotonation, nucleophilic attack, electron transfer, or substitution of a neutral diimine with an anion. This paper focuses on the ion pairs and their charge-reduction products. The former we now describe in detail.

Intra- and intermolecular forces in ion pairs

Our MS data highlight the reactivity of the salt mixtures under the duress of ESI and collisions with N_2 . To evaluate relative stabilities and confirm reaction channels of ion pairs, we conduct CID with tandem mass spectrometry (MS/MS). We select the parent ion pairs {[Ru(N^N)₃]X} $^+$ with a quadrupole, collide them into Ar, and then

Article



separate the cationic products in a time-of-flight (TOF) analyzer. We plot the fraction of parent ions intact as a function of collision energy to obtain breakdown curves. In favorable cases, CID of {[Ru(N^N)_3]X}⁺ gives a sigmoidal curve, and we can estimate the collision energy required for 50% dissociation ($CE_{1/2}$; Table S2), a useful relative metric of stability. The following focuses on ion pairs featuring [Ru(bipy)_3]²⁺ or [Ru(phen)_3]²⁺. We find intermediate behavior for [Ru(bipy)_2(phen)]²⁺ and do not describe it in detail here (Figures S68–S96). Our discussion is organized according to the anions involved.

${[Ru(N^N)_3]F}^+$, ${[Ru(N^N)_3]Cl}^+$, and ${[Ru(N^N)_3]Br}^+$

We begin with the smallest and most basic halide, F^- , whose high charge density should see it bind $[Ru(N^N)_3]^{2+}$ dications strongly. However, the reactivity of F^- , including toward solvents, lets us observe $\{[Ru(bipy)_3]F\}^+$ (Figures S4 and S5) and $\{[Ru(bipy)_2(phen)]F\}^+$ (Figure S71) only in very low abundance and $\{[Ru(phen)_3]F\}^+$ not at all. The ion pair $\{[Ru(bipy)_3]F\}^+$ is fragile ($CE_{1/2}=0.2\ V$; Figure 3A) and loses HF to give $[Ru(bipy)_2(bipy-H)]^+$, which loses bipy to give $[Ru(bipy)(bipy-H)]^+$. Even more facile is bipy extrusion from the ion pair to give $[Ru(bipy)_2F]^+$. In both cases, Ru loses ligands because it is compensated by (1) an anion moving from the outer to the inner sphere or (2) a remaining diimine N^N getting converted into a more basic anionic derivative such as $[N^N-H]^-$. We see similar chemistry for $\{[Ru(bipy)_2(phen)]F\}^+$, whose fragmentation tells us that loss of bipy is more facile than loss of phen (Figures S70 and S71).

Ruthenium diimines are readily available as their Cl⁻ salts, so the interactions between $[Ru(N^N)_3]^{2+}$ and Cl^- are of practical relevance. CID of $\{[Ru(bipy)_3]Cl\}^+$ $(CE_{\frac{1}{2}} = 1.4 \text{ eV})$ sees it lose bipy to give $[Ru(bipy)_2Cl]^+$ or lose Cl^- to give the dication [Ru(bipy)₃]²⁺ (Figures 3B and S7). The latter "ionic" bond cleavage is trivial in dielectric solvents but rarely dominates in the gas phase. At high energies, [Ru(bipy)₂Cl]⁺ eliminates HCl to give [Ru(bipy)(bipy-H)]⁺, a fragment that could also arise should [Ru(bipy)₃]²⁺ extrude [bipyH]⁺—a Coulombic fission that sees a dication convert into two monocations. The analog {[Ru(phen)₃]Cl}⁺ (Figures 3C and S41) is more robust than {[Ru(bipy)3]Cl}+ and loses phen only at higher energies. Ligated phen is less acidic than bipy, so we get a simple breakdown curve for {[Ru(phen)₃]Cl}⁺ $(CE_{1/2} = 6.7 \text{ eV})$. The bromide $\{[Ru(bipy)_3]Br\}^+$ (Figures S9 and S10; $CE_{1/2} = 3.6 \text{ eV}$) gives similar CID products to {[Ru(bipy)₃]Cl}⁺, albeit with less deprotonation. In the case of {[Ru(phen)₃]Br}⁺, we get smooth phen loss that mirrors that of the Cl⁻ ion pairs. Loss of bipy is more facile than phen and can be accompanied by HBr loss. Like {{Ru(phen)₃]Cl}⁺, {{Ru(phen)₃]Br}⁺ undergoes only phen loss, so the ion pair and {[Ru(phen)₂Br]⁺ are the only intense ions over a range of collision energies (Figures S43 and S44; $CE_{1/2} = 8.8 \text{ eV}$).

${[Ru(N^N)_3]I}^+$

HX loss from {[Ru(bipy)₃]Cl}⁺ is faster than it is from {[Ru(bipy)₃]Br}⁺ and does not occur at all from the iodide ion pairs {[Ru(bipy)₃]l}⁺ ($CE_{1/2} = 7.7$ eV) or {[Ru(phen)₃] l}⁺ ($CE_{1/2} = 11.1$ eV). These extrude N^N but do not dehydrohalogenate; they instead exhibit electron transfer, as elimination of I• gives reduced species [Ru(N^N)₃]⁺ (Figures 4, S13, and S46). We will describe these topical cations below; for now, we note that I loss is the reverse of a harpoon reaction, $^{23-25}$ with the loss of anions as corresponding neutral radicals being common in MS.

${[Ru(N^N)_3]PF_6}^+$

Relative to the halide salts, $[Ru(N^N)_3](PF_6)_2$ can be more desirable because it is amenable to photoredox catalysis in polar organic solvents. Yet, the lability of



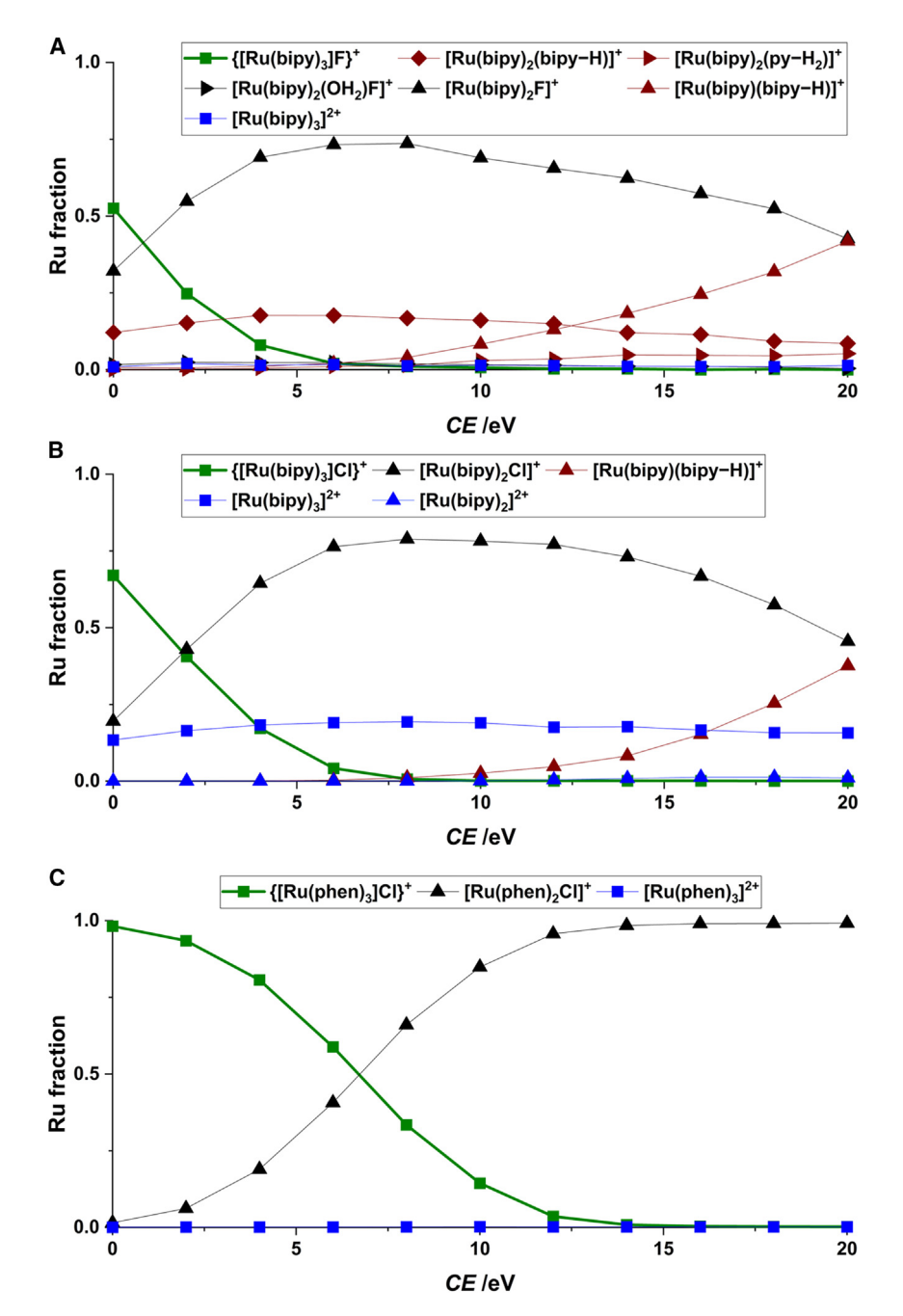


Figure 3. CID of fluorides is quite distinct to the more robust chloride ion pairs

- (A) $\{[Ru(bipy)_3]F\}^+$ initially loses bipy or HF.
- (B) {[Ru(bipy)₃]Cl}⁺ primarily loses bipy or Cl⁻.
- (C) {[Ru(phen)₃]Cl}⁺ almost exclusively loses phen.

PF₆⁻ itself should not be underestimated, ¹⁰ and CID of {[Ru(bipy)₃]PF₆}⁺ results mostly in loss of bipy and PF₅ to give [Ru(bipy)₂F]⁺ (Figures S17 and S18; $CE_{1/2} = 13.5$ eV). The other major channel affords [Ru(bipy)₂(bipy–H)]⁺ and HPF₆, though it is unclear whether intact PF₆⁻ or F⁻ is the base. The analog {[Ru(phen)₃]PF₆}⁺ is more robust but affords similar products (Figures S48–S50; $CE_{1/2} = 21.6$ eV), with the main difference being that phen extrusion to give [Ru(phen)₂F]⁺ is slow, such that deprotonation to give [Ru(phen)₂(phen–H)]⁺ and HPF₆ dominates instead.



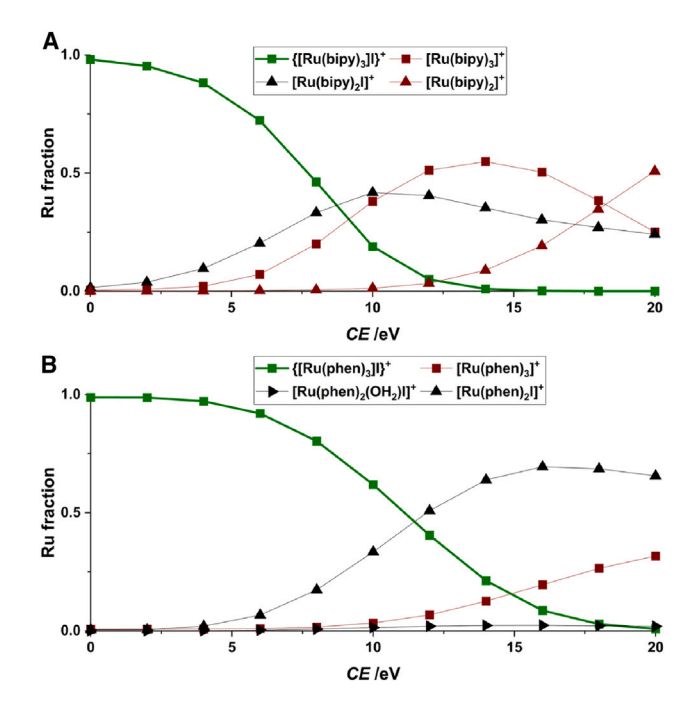


Figure 4. lodide is redox active, so its ion pairs undergo diverse chemistry (A) CID of {[Ru(bipy)₃]I}* results principally in bipy loss and/or I loss. (B) {[Ru(phen)₃]I}* exhibits similar reactivity but is more robust.

${[Ru(N^N)_3]O_2CH}^+$

Our interest in formates {[Ru(N^N)_3]O_2CH}^+ comes from $^-$ O_2CH being an important intermediate in carbon cycles. 26 {[Ru(bipy)_3]O_2CH}^+ is labile ($CE_{1/2}$ = 1.7 eV) and even at low energies extrudes either bipy to give [Ru(bipy)_2(O_2CH)]^+ or CO_2 to give [Ru(bipy)_2(bipyH)]^+ (Figures 5A and S20).

The regiochemistry of the hydride addition that affords the [bipyH]⁻ ligand is unclear. DFT calculations suggest that attack at C4 is 0.14 eV more thermodynamically favorable (Figure S101) than at C6 (Figure S102). At high collision energies, [Ru(bipy)₂(bipyH)]⁺ and [Ru(bipy)₂(O₂CH)]⁺ lose bipyH₂ and HO₂CH, respectively, to give [Ru(bipy)(bipy–H)]⁺. We even see C2–C2' scission of bipy to afford the putative ligand NC₅H₂⁻, which may be a dehydrogenated pyridyl anion ruthenated at C2 or may couple to bipy to form a larger ligand. The competing hydride addition and deprotonation channels reflect the hydricity and basicity of $^-$ O₂CH. A common theme here is that Ru^{||} binds phen so tightly that ligand-centered reactions predominate, even though phen is less reactive than bipy. So {[Ru(phen)₃]O₂CH}⁺ converts into [Ru(phen)₂(phenH)]⁺ (Figures 5B and S53; $CE_{1/2} = 1.3$ eV), which at higher energies loses phen to give [Ru(phen)(phenH)]⁺. A plausible alterative reaction channel, which we did not observe, would see the imine-amido ligand [phenH]⁻ in [Ru(phen)₂(phenH)]⁺ deprotonate a phen in the same complex to give phenH₂ (putatively 1,2-dihydro-1,10-phenanthroline) and [Ru(phen)(phen-H)]⁺.

${[Ru(N^N)_3]OAc}^+$

The carboxylates $^{-}O_2CH$ and ^{-}OAc have comparable basicities, but the latter is not a hydride source. Instead, $\{[Ru(bipy)_3]OAc\}^+$ ($CE_{\frac{1}{2}}=2.3$ eV) loses either (1) HOAc to give $[Ru(bipy)_2(bipy-H)]^+$ or (2) bipy to give $[Ru(bipy)_2(OAc)]^+$. Both $[Ru(bipy)_2(bipy-H)]^+$ and $[Ru(bipy)_2(OAc)]^+$ can turn into $[Ru(bipy)(bipy-H)]^+$ or undergo C2-C2' bipy scission (Figures 6A and S24). CID of the phen analog



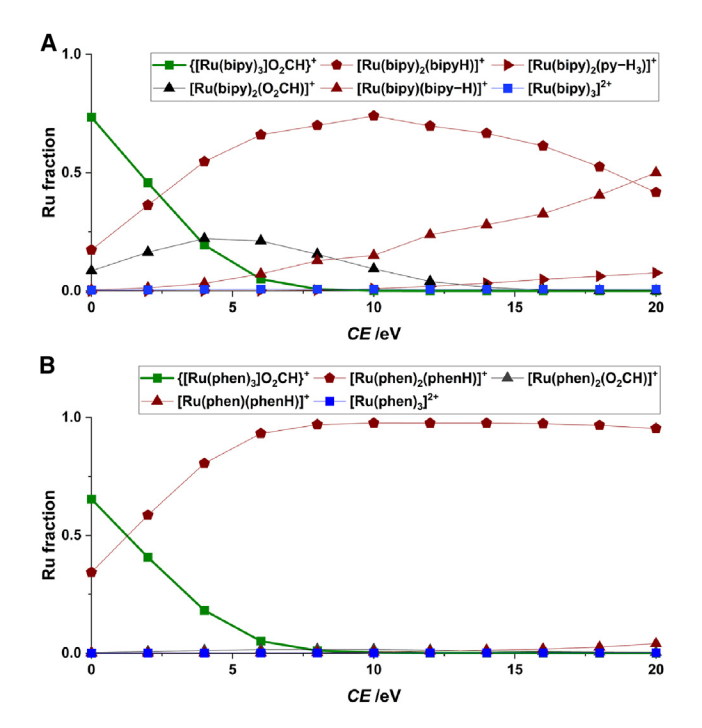


Figure 5. Formates undergo facile CID and primarily lose CO_2 (A) {[Ru(bipy)₃]O₂CH}⁺ mostly loses CO_2 to give [Ru(bipy)₂(bipyH)]⁺, which further loses bipyH₂. (B) {[Ru(phen)₃]O₂CH}⁺ gives [Ru(phen)₂(bipyH)]⁺, which is robust.

 $\{[Ru(phen)_3]OAc\}^+$ is dominated by the first diimine-centered reaction channel (Figures 6B and S57; $CE_{1/2} = 5.8$ eV), with preferential loss of HOAc at all collision energies giving $[Ru(phen)_2(phen-H)]^+$. This reaction is unusual because phen is not amenable to rollover, making the regiochemistry unclear.

${[Ru(N^N)_3]BAr_4}^+$

Ruthenium diimines are often used as tetraarylborate salts because these anions confer solubility in many organic solvents.²⁷ However, association between the heavy aromatic cations and anions in the gas phase is strong because solvent cannot interfere with the electrostatic, van der Waals, and π – π interactions. Here, tetraarylborates $\{[Ru(N^N)_3]BAr_4\}^+$ do not dissociate into $[Ru(N^N)_3]^{2+}$ and BAr_4^- ions we would see in solution but rather into charge-reduction products. Thus, {[Ru(N^N)₃] BPh₄}⁺ species give reduced complexes [Ru(N^N)₃]⁺ through an electron transfer analogous to that in {{Ru(N^N)₃}|}⁺ (Figures 7, S28, S29, and S62). Aside from electron transfer, two minor CID channels see Ph⁻ deprotonate or add to diimines, in the latter case giving $[Ru(N^N)_2(N^NPh)]^+$ (Figure 2, top left), which features the arylated dearomatized ligand N^NPh⁻. The arylation regiochemistry is unclear, but C4 attack seems likely based on steric availability and analogy with hydride attack. Moving from BPh₄⁻ to the poorer reductant BAr^F₄⁻ sees deprotonation and arylation dominate the CID of {[Ru(bipy)₃]BAr^F₄}⁺ (Figures S31 and S32; $CE_{1/2} = 53.8 \text{ eV}$). Lastly, the phen analog $\{[Ru(phen)_3]BAr_4^F\}^+$ gives reduced species $[Ru(phen)_2]^+$, perhaps via [Ru(phen)₃]⁺, because anylation of phen is far slower than bipy (Figures S64–S67; $CE_{1/2} = 68.8 \text{ eV}$).

Tetraarylborates are robust, but $[H(OEt_2)_2]BAr^F_{4}$, for example, decomposes into the arene HAr^F and borane BAr^F_{3} , which is analogous to aryls deprotonating coordinated N^N. As for arylations of diimines, $[Ru(N^N)_2(N^NAr)]^+$ could form by two



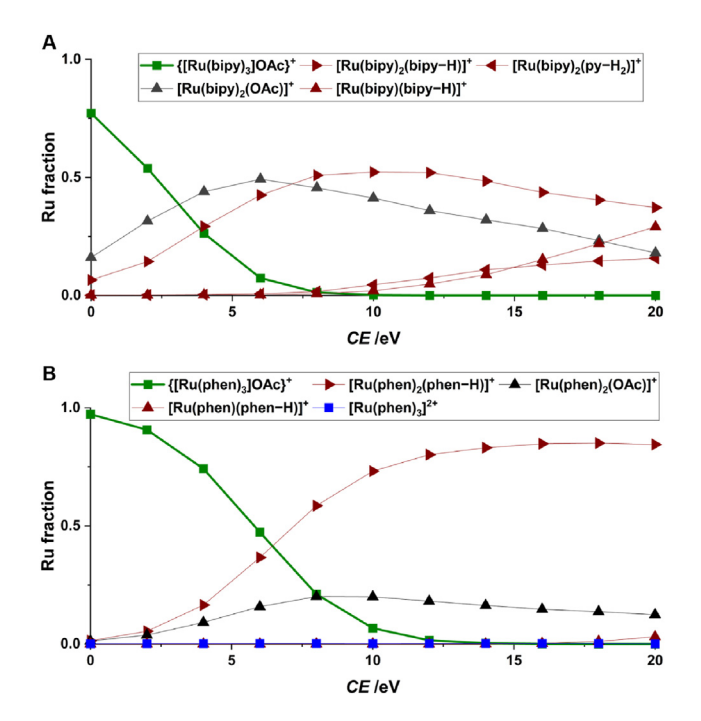


Figure 6. CID of acetate ion pairs highlights acid-base non-innocence

(A) {[Ru(bipy)₃]OAc}⁺ eliminates HOAc or bipy.

(B) {[Ru(phen)₃]OAc}⁺ also loses HOAc but loses phen to a lesser degree.

mechanisms: (1) aryl anion transfer or (2) electron transfer followed by radical addition. The second route, $[Ru(N^{N})_{3}]^{2^{+}} + BAr_{4}^{-} \rightarrow [Ru(N^{N})_{3}]^{+} + BAr_{4}^{-} \rightarrow [Ru(N^{N})_{2}(N^{N})_{3}]^{+} + R^{+} \rightarrow [Ru(N^{N})_{2}(N^{N})_{2}(N^{N})_{3}]^{+} + R^{+} \rightarrow [Ru(N^{N})_{2}(N^{N})_{3}]^{+} + R^{+} \rightarrow [Ru(N^{N})_{2}(N^{N})_{2}(N^{N})_{3}]^{+} + R^{+} \rightarrow [Ru(N^{N})_{2}(N^{N})_{3}]^{+} + R^{+} \rightarrow [Ru(N^{N})_{3}]^{+} + R^{+} \rightarrow [Ru(N^{N})_{3}]^{+} + R^{+} \rightarrow [Ru(N^{N})_{2}(N^{N})_{3}]^{+} + R^{+} \rightarrow [Ru(N^{N})_{2}(N^{N})_{3}]^{+} + R^{+} \rightarrow [Ru(N^{N})_{2}(N^{N})_{3}]^{+} + R^{+} \rightarrow [Ru(N^{N})_{3}]^{+} + R^{+} \rightarrow [Ru(N^$

Charge-reduction products

Our MS/MS measurements showed how the ion pairs {[Ru(N^N)_3]X}+ undergo dissociation of (outer-sphere) ionic bonds or (inner-sphere) Ru–N bonds, as well as ligand-centered reactions (Figure 2). To see what drives deprotonation and ruthenation, for each ion pair {[Ru(N^N)_3]X}+, we summed the abundances of [Ru(N^N)_n(N^N-H)]^+ (n=1,2) at the same collision energy (20 eV; Table S3 and Figure S97). The extent of deprotonation correlates with (1) proton affinity²⁹ of X⁻ and (2) number of bipy ligands, which are more acidic than phen. Anomalies exist because deprotonation competes with other channels. Relative to deprotonation, the electron transfer {[Ru(N^N)_3]X}^+ \rightarrow [Ru(N^N)_3]^+ + X channel is less prominent and with the halides only in the case of I⁻ because the electron affinity of I (3.06 eV)³⁰ is much less than that of Br (3.36 eV),³¹ Cl (3.61 eV),³² and F (3.40 eV).³¹ Our MS/MS data for {[Ru(N^N)_3]}^+ reveal substantial formation of [Ru(N^N)_3]^+, the relative



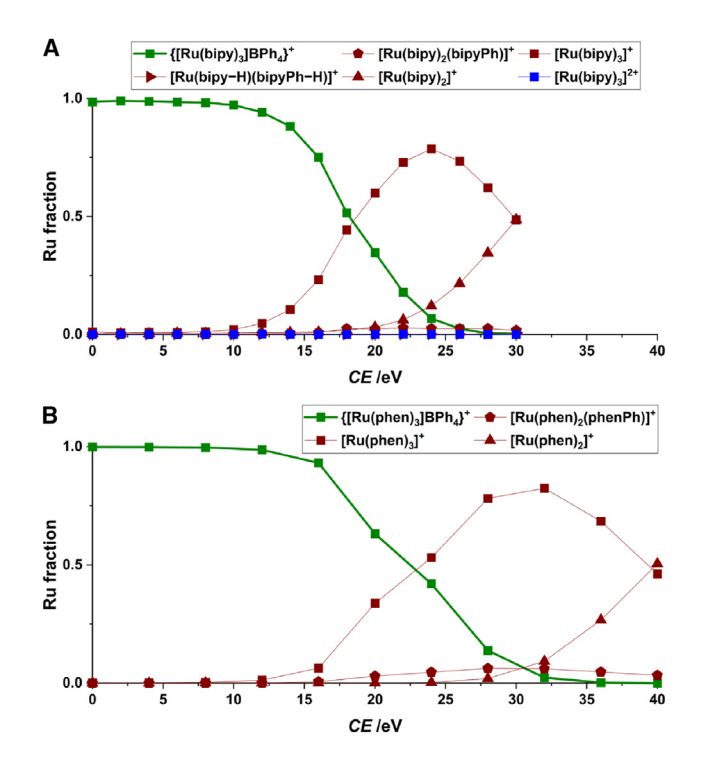


Figure 7. Tetraphenylborate ion pairs are surprisingly robust
(A) {[Ru(bipy)₃]BPh₄}⁺ undergoes interion electron transfer.
(B) {[Ru(phen)₃]BPh₄}⁺ exhibits similar chemistry but at higher collision energies.

abundance of which decreases in an order $[Ru(bipy)_3]^+$ (0.76) > $[Ru(bipy)_2(phen)]^+$ (0.44) > $[Ru(phen)_3]^+$ (0.32) consistent with standard potentials ($E([Ru(bipy)_3]^{2+/+}) = -1.31 \text{ V}^{33}$ and $E([Ru(phen)_3]^{2+/+}) = -1.35 \text{ V}$ versus saturated calomel electrode). BPh₄⁻ and BAr^F₄⁻ also reduce dications but only at high energies less relevant to catalysis.

Complexes of anionic bipyridine derivatives

Notable among ligand-centered reaction products (Table S1, maroon entries) is our series $[Ru(bipy)_2(bipyH)]^+$ (m/z 571), $[Ru(bipy)_2(bipy•)]^+$ (m/z 570), and $[Ru(bipy)_2(bipy-H)]^+$ (m/z 569), which differ only by H atoms. These complexes feature anionic ligands [bipyH]⁻ (from hydride addition), [bipy•]⁻ (from electronation), and [bipy-H]⁻ (from deprotonation and rollover). Here, we have an opportunity to compare complexes of underexplored anionic bipy variants. We noted above that [Ru(bipy)₂(bipyH)]⁺ is the product of hydride attack, most likely at a C4 or C6 site. The main CID channel for this complex sees its [bipyH] ligand deprotonating bipy to liberate [Ru(bipy)(bipy-H)]⁺ and bipyH₂ (Figures 8A, S21, and S22; py = pyridine; $CE_{1/2}$ = 17.1 eV). CID tells us that bipyH₂ binds Ru more weakly than does bipy or [bipy-H]⁻, suggesting that bipyH₂ is likely hydrogenated at the N and C4 or C6 atoms. The reaction that gives bipyH2 is similar to the bimolecular aqueousphase reaction $[Ru(bipy)_2(bipyR)]^+ + H_2O \rightarrow [Ru(bipy)_2(bipyRH)]^{2+} + OH^-$, in which alkylated anion bipyR⁻ undergoes protonation.⁵ Less-important reactions of [Ru(bipy)₂(bipyH)]⁺ are loss of hydride and [bipyH]⁻ scission. Relative to [Ru(bipy)₂(bipyH)]⁺, the analog [Ru(phen)₂(phenH)]⁺ dissociates more cleanly but gives [Ru(phen)(phenH)]⁺ and phen rather than [Ru(phen)(phen-H)]⁺ and phenH₂ (Figures S53–S55; $CE_{\frac{1}{2}}$ = 27.0 eV) because [phenH]⁻ is too rigid to be an internal Brønsted base like [bipyH]-.



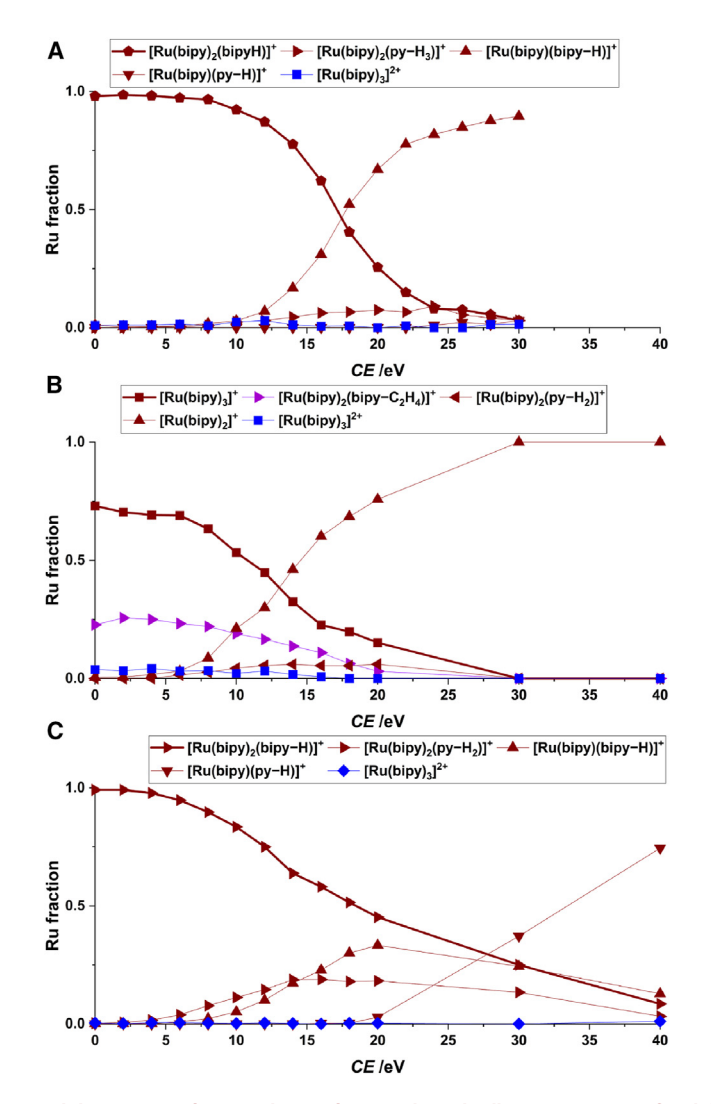


Figure 8. Breakdown curves for complexes of anionic ligands allow comparison of stabilities

- (A) $[Ru(bipy)_2(bipyH)]^+$ cleanly loses $bipyH_2$.
- (B) $[Ru(bipy)_2(bipy \cdot)]^+$ is labile and readily loses bipy and/or fragments thereof.
- (C) $[Ru(bipy)_2(bipy-H)]^+$ is more robust and affords species with deprotonated heterocycles.

The radical [Ru(bipy)₃]⁺ (Figures 8B, S14, and S15; $CE_{1/2} \approx 10.9 \text{ eV}$) is more labile than dication [Ru(bipy)₃]²⁺ (Figures S2 and S3; $CE_{1/2} = 26.4 \text{ eV}$). These results qualitatively agree with previous DFT studies that show the activation energy for bipy extrusion from [Ru(bipy)₃]⁺ ($E_a = 2.57 \text{ eV}$, M06/TZ2P; $E_a = 2 \text{ eV}$, B3LYP/def2-TZVP)³⁵ to be less than that for [Ru(bipy)₃]²⁺ ($E_a = 4.54 \text{ eV}$, M06/TZ2P).³⁶ Although both reactions see cleavage of two Ru^{II}–N bonds, we reconcile the E_a differences in terms of charge-transfer from [bipy•]⁻ to Ru^{II}, which lessens the impact that Ru experiences on losing bipy. Thus, [Ru^{II}(bipy)₂(bipy•)]⁺ \rightarrow [Ru^{II}(bipy)₂]²⁺ + bipy is more facile than is [Ru^{II}(bipy)₃]²⁺ \rightarrow [Ru^{II}(bipy)₂]²⁺ + bipy, because Ru in the latter product is more electron-poor.

The last complex in our series, $[Ru(bipy)_2(bipy-H)]^+$, dissociates through C2–C2′ scission of the $[bipy-H]^-$ ligand or loss of bipy (Figures 8C, S25, and S26; $CE_{1/2} = 18.6$ eV). At higher energies, these processes are sequential and give $[Ru(bipy)(py-H)]^+$, which putatively bears a 2-pyridyl anionic ligand. Overall,



Table 1. MS-IMS-MS data, computed binding energy, average radius of gyration, and standard deviation for selected monocations							
lon	m/z	t _d /ms	CCS _{exp} /Å ²	CCS _{calc} /Å ²	E _b /eV	< <i>R</i> _g >/Å	$\sigma(R_{\rm g})/{\rm \AA}$
[Ru(bipy) ₂ (bipy-H)] ⁺	569	6.18	215.3	N/D	N/D	N/D	N/D
[Ru(bipy) ₃] ⁺	570	6.37	215.6	N/D	N/D	N/D	N/D
{[Ru(bipy) ₃]Cl} ⁺	605	6.55	223.2	238.4	-6.17	4.24	0.019
{[Ru(bipy) ₃]Br}+	649	6.74	225.5	238.9	-5.73	4.28	0.018
{[Ru(bipy) ₃]I} ⁺	697	6.93	228.6	248.1	-5.44	4.35	0.025
{[Ru(bipy) ₃]O ₂ CH} ⁺	615	N/D	N/D	240.8	-5.47	4.28	0.024
{[Ru(bipy) ₃]OAc} ⁺	629	6.93	229.7	245.4	-5.35	4.47	0.047
{[Ru(bipy) ₃]PF ₆ }+	715	7.30	236.7	N/D	N/D	N/D	N/D
{[Ru(bipy) ₃]BPh ₄ }+	889	10.49	293.9	N/D	N/D	N/D	N/D
[Ru(phen) ₂ (phen-H)] ⁺	641	7.12	234.3	N/D	N/D	N/D	N/D
[Ru(phen) ₃] ⁺	642	7.12	234.1	N/D	N/D	N/D	N/D
{[Ru(phen) ₃]Cl}+	677	7.49	239.8	N/D	N/D	N/D	N/D
{[Ru(phen)3]Br}+	721	7.68	242.1	N/D	N/D	N/D	N/D
{[Ru(phen) ₃]I}+	769	7.68	244.6	N/D	N/D	N/D	N/D
{[Ru(phen) ₃]OAc} ⁺	701	7.87	246.6	N/D	N/D	N/D	N/D
{[Ru(phen) ₃]PF ₆ }+	787	8.24	253.3	N/D	N/D	N/D	N/D
{[Ru(phen) ₃]BPh ₄ }+	961	11.05	305.6	N/D	N/D	N/D	N/D

 CCS_{exp} values correlate with average radii of gyration $< R_g >$ determined from MD, as well as with CCS_{calc} values predicted from static DFT structures. N/D, not determined.

the thermal stabilities for our series fall in the order $[Ru(bipy)_2(bipy-H)]^+ \approx [Ru(bipy)_2(bipy+)]^+ > [Ru(bipy)_2(bipy+)]^+$. The phen analogs $[Ru(phen)_2(phenH)]^+$ (Figures S53, S54, and S55) and $[Ru(phen)_2(phen-H)]^+$ (Figures S58, S59, and S60) are more stable but do cleanly lose phen at high energies. Overall, complexes of the dearomatized ligands $[N^NH]^-$ are about as stable as those of deprotonated ligands $[N^N-H]^-$ and are more stable than those of the radical $[bipy+]^-$, a more common ligand. Again, we posit that this is because the latter ligand engages in charge transfer to Ru^{II} , while the former do not.

Intra- and even intermolecular forces can be strong in the gas phase, as evidenced by the many charge-reduction processes we observe. Given the high energies at which many of these occur, we now study the ion pairs $\{[Ru(N^N)_3]X\}^+$ without imparting collision energy to learn about ruthenium diimines under conditions more relevant to catalysis.

Structures and dynamics of ion pairs

Ion mobility spectrometry

To learn about the structures and dynamics of example $\{[Ru(N^N)_3]X\}^+$ ion pairs, as well as deprotonated $[Ru(N^N)_2(N^N-H)]^+$ and reduced species $[Ru(N^N)_3]^+$, we selected the ion pairs and subjected them to traveling-wave IMS, whereby we measure the time it takes a traveling voltage wave to propel ions through a N_2 -filled mobility cell before MS detection. This overall MS-IMS-MS workflow afforded us peak arrival times (t_d , Tables 1 and S4 and Figures S98–S100), which we converted into experimental collision cross-section (CCS_{exp}) values. CCS_{exp} for $\{[Ru(N^N)_3]X\}^+$ increases with increasing size of $X^{-,38}$ such that $\{[Ru(N^N)_3]BPh_4\}^+$ ion pairs are the largest, followed by $\{[Ru(N^N)_3]PF_6\}^+$ and $\{[Ru(N^N)_3]OAc\}^+$. We conclude that halides do not protrude much from the pockets between diimines, particularly the large phen ligands, as is corroborated in DFT structures (see below). These halide ion pairs are only marginally larger than the radical cations $[Ru(N^N)_3]^+$, which, in turn, are similar in size to deprotonated species $[Ru(N^N)_2(N^N-H)]^+$. Although the differences are small, $[Ru(bipy)_2(bipy-H)]^+$ being smaller than $[Ru(bipy)_3]^+$ is consistent with rollover metalation removing H^+ protruding from a

Article



C3 site. In contrast, $[Ru(phen)_2(phen-H)]^+$ and $[Ru(phen)_3]^+$ have very similar arrival times, consistent with deprotonation at a C2 site adjacent to an N atom, which would barely affect CCS. In general, t_d values for an ion have a distribution, the breadth of which is related to the intrinsic structural variability of an ion but also experimental aspects like the number of ions pushed from our quadrupole to the ion mobility cell and longitudinal diffusion (Figures S98 and S100). Thus, we do not make inferences between breadth and fluxionality here. To learn more about these dynamics, we instead turn to computational chemistry.

DFT-calculated structures

We performed DFT calculations to get minimum-energy structures of the halides $\{[Ru(bipy)_3]Cl\}^+$, $\{[Ru(bipy)_3]Br\}^+$, and $\{[Ru(bipy)_3]D^+\}$, as well as the carboxylates $\{[Ru(bipy)_3]O_2CH\}^+$ and $\{[Ru(bipy)_3]O_4C\}^+$ (Figures S103–S107; Tables S5–S9). These structures allow us to implement a trajectory method and Lennard-Jones potential to predict CCS_{calc} (Table 1), with the resulting values being consistent with our measurements. This supports our model that $\{[Ru(bipy)_3]X\}^+$ species indeed are ion pairs rather than covalent adducts, such as those that would arise from the anion attacking the diimine. We also got binding energies $(E_b; Table 1)$ of the ion pairs relative to separated $[Ru(bipy)_3]^{2+}$ and X^- . For halides, the strength of binding decreases with increasing effective ionic radius (1.81, 1.96, and 2.20 Å for Cl^- , Br^- , and l^- , respectively), in line with Coulomb's law. Similarly, the higher charge density of HCO_2^- compared to AcO^- is responsible for the stronger binding (i.e., more negative E_b) of the former.

MD of ion pairs

We simulated MD trajectories over 25 ps for each canonical ensemble—the ion pair and a heat bath used to fix the temperature at 300 K. The center of mass of each ion pair depends on the location of the anion, so we reasoned that the difference in size between the ion pairs would be reflected in the radius of gyration $R_{\rm g}$. In each case, $R_{\rm g}$ fluctuates (Figure 9A; Videos S1 and S2), so it is useful to consider its frequency distribution (Figure 9B).

The time-averaged values $< R_g >$ (Table 1) fall in the same order as t_d and CCS (Table 1). Further, the $< R_g >$ values predict t_d of $\{[Ru(bipy)_3]O_2CH\}^+$ to be similar to that of $\{[Ru(bipy)_3]Br\}^+$. We interpret the standard deviation $\sigma(R_g)$ as a measure of size variability (Table 1). Thus, while this value is similar for $\{[Ru(bipy)_3]Br\}^+$ (0.018 Å) and $\{[Ru(bipy)_3]Cl\}^+$ (0.019 Å), it is greater in the case of $\{[Ru(bipy)_3]D\}^+$ (0.025 Å) because this latter ion pair is more flexible. The contrast in $\sigma(R_g)$ is more striking for carboxylates $\{[Ru(bipy)_3]O_2CH\}^+$ (0.025 Å) and $\{[Ru(bipy)_3]OAc\}^+$ (0.047 Å) because AcO^- is larger and induces surprisingly large geometric distortions in the bipy ligands. Both carboxylates engage in $O\cdot\cdot\cdot H$ –C interactions with $[Ru(bipy)_3]^{2+}$, as illustrated by the number of hydrogen bonds between the ions over the MD trajectory. The average number of hydrogen bonds in $\{[Ru(bipy)_3]O_2CH\}^+$ (2.49; Figure S108) is higher than that in $\{[Ru(bipy)_3]OAc\}^+$ (2.34; Figure S109) because hydrogen bond formation is sterically hindered in the latter. This hindrance toward forming a more stable static structure may be why the acetate experiences large structural changes.

When subjected to high-energy collisions, ruthenium diimine ion pairs undergo diverse gas-phase reactions dominated by charge reduction. Such pathways, which depend greatly on the basicity and reducing power of the anion, include ligand-centered reactions that give topical anionic ligands. Much has been made of redox and (to a lesser extent) acid-base non-innocence of coordinated diimines, but less is



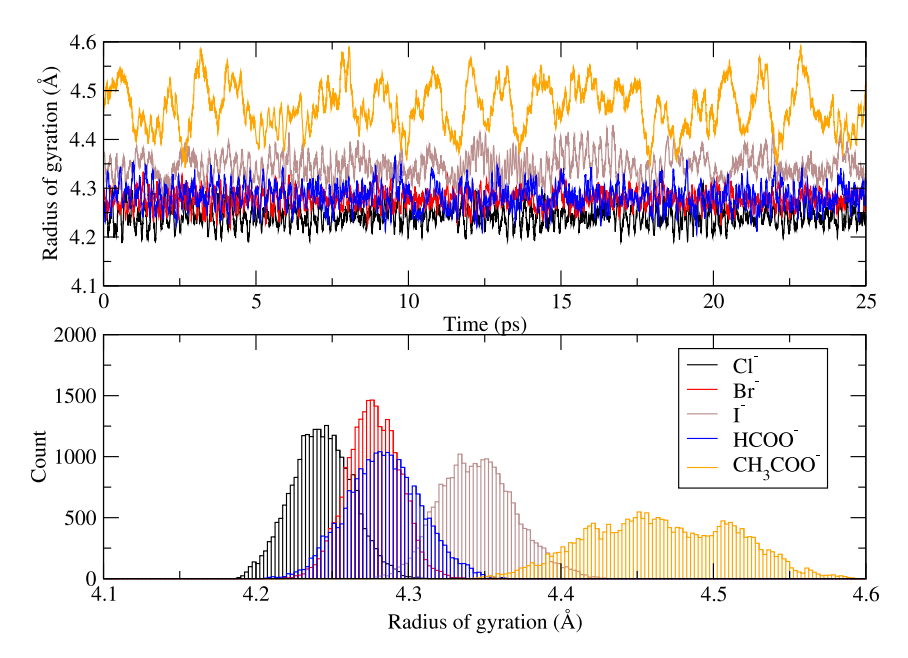


Figure 9. Ion pairs are highly fluctional on the picosecond timescale

(A) $\{[Ru(bipy)_3](OAc)\}^+$ features hydrogen bonding and samples the fewest geometries, in contrast to $\{[Ru(bipy)_3]CI\}^+$.

(B) The ion pairs exhibit different size distributions.

known about their susceptibility to hydride attack. This underscores the importance of our detection of anionic diimine derivatives, especially hydride adducts relevant to hydrogen evolution. At lower energies, the ion pairs persist, so we can learn their relative sizes by IMS, which agree with those determined by MD simulations. The latter paint a picture of ion pair flexibility, which is greatest for larger ion pairs and least for smaller ones. Information from MS can be relevant to bulk reactions because internal energy distributions in CID are qualitatively similar to thermal energy distributions.³⁹ However, there are caveats that come with extending lessons from gasphase studies to bulk solution, where most photoredox catalysis is conducted. First, our ions are dilute, desolvated, and often subjected to large collision energies. Second, we only detect charged species. It is for this reason that we used dicationic complexes, so even when charge reduction occurs, we still see monocationic fragments and can infer the identity of neutral species lost. The basicity and reducing power of most anions we use in photocatalysis are not usually considered to be strong enough to influence reactivity. A key lesson we present here is that we should not underestimate this reactivity, steering clear of certain anions (e.g., I⁻ and AcO⁻) if we want Ru diimines to maintain their integrity.

Overall, MS is a sensitive approach that yields detailed information about the innerand outer-coordination spheres of diimine complexes, which may guide us toward more effective photosensitizers. Our experimental and theoretical case study is generalizable to ion pairs in general. All we need is for the ion pairs to be charged, a condition best met when the magnitudes of the constituent ionic charges are nonequal.

EXPERIMENTAL PROCEDURES

Resource availability

Lead contact

Requests for further information should be directed to and will be granted by the lead contact, Dr. David Schilter (schilter@txstate.edu).

Cell Reports Physical Science Article



Materials availability

This study did not generate new materials.

Data and code availability

Any additional information required to reanalyze the data reported in this paper is available from the lead contact on request.

Experimental details

The racemic salts $[Ru(bipy)_3]Cl_2$ and $[Ru(phen)_3]Cl_2$, ⁴⁰ $[Ru(bipy)_2(phen)]Cl_2$, ⁴¹ and $[Ru(bipy)_3](BAr^F_4)_2$ were prepared as previously reported. Stock solutions were prepared using HPLC-grade MeOH and MeCN and deionized/millipore-filtered H₂O. $[Ru(N^N)_3]Cl_2$ (10 mM in H₂O), nBu_4NX ($X^- = F^-$, Br^- , I^- , PF_6^- , AcO^- ; 10 mM in H₂O), NaX ($X^- = BPh_4^-$ and $BAr^F_4^-$; 10 mM in MeOH), and NaO₂CH/HO₂CH buffer (NaOH [0.4 mg, 10 µmol], HO₂CH [20 µL, 0.53 mmol] in H₂O [4.3 mL], and MeCN [16 mL]) solutions were prepared and stored in a refrigerator.

Solutions for MS were prepared by diluting stock solutions of [Ru(N^N)₃]Cl₂ (5 μ L × 10 mM) and the anion X⁻ (10 μ L × 10 mM) with MeOH (985 μ L), such that [[Ru(N^N)₃]²⁺] = 50 μ M and [X⁻] = 100 μ M. A syringe pump infused these solutions (10 μ L min⁻¹) into a Waters Synapt XS ion mobility mass spectrometer, in which ESI-generated ions encounter a resolving quadrupole, traveling-wave ion mobility cell, and then a TOF analyzer. Data were acquired in high-resolution positive-ion mode with cone of 10 V, source offset of 4.5, source of 80°C, and N₂ desolvation temperature of 200°C.

MS data were acquired at different capillary voltages over the range 0.31–1.51 kV. MS/MS data were acquired at a capillary voltage of 1.25 kV, acquiring scans at different transfer collision energies until all parent ions dissociated. The low-mass resolution of the quadrupole was typically ~4, whence most isotopologs of the parent ions were transmitted. The resolution was increased up to 15 if necessary to ensure the parent ion was pure. 10 MS scans were acquired at each capillary voltage, and 10 MS/MS scans were acquired at each transfer collision energy. The spectra were combined and integrated in MassLynx v4.2. For MS-IMS-MS, we used a capillary voltage of 1.07 kV and a low-mass resolution of 15 to select the most intense isotopologs of the parent ion envelope to enter the N2-filled mobility cell. The final mobiligrams depict elution of the most intense isotopolog. The wave velocity was $4.6~\mathrm{ms}^{-1}$, and the wave height was either $43.1~\mathrm{V}$ (data presented here) or 24.7 V (data presented in the supplemental information). In each case, 117 scans were acquired and allowed conversion of arrival times t_d into CCS using DriftScope v3.0. Selected measurements were repeated after 1 week, with no change in t_d. We calibrated our instrument with a solution containing succinic acid, salicylic acid, theophylline, pantothenic acid, stearic acid, perfluoroheptanoic acid, perfluorooctanoic acid, perfluorononanoic acid, perfluorodecanoic acid, perfluorododecanoic acid, poly(DL-alanine), and ultramark 1621 in MeCN-H₂O (1:1) + 0.089% HCO₂H. These species form ions with known CCS values.³⁸

Computational details

DFT calculations were performed on the QUICKSTEP program within the CP2K package, ⁴³ using GTH pseudopotentials. ⁴⁴ We used the Perdew-Burke-Ernzerhof functional and DZVP-MOLOPT basis set. ⁴⁶ We did not set any periodicity. The geometry optimizations relied on a limited memory algorithm (LBFGS) with a force convergence criterion of 0.02 eVÅ⁻¹. DFT-based MD simulations were started from the optimized structures, which we equilibrated for 3 ps to converge the



potential energy (Figure S110) in the NVT ensemble with a Nosé-Hoover thermostat 48 set at 300 K. We used a time step of 0.5 fs to integrate the equations of motion. We count O···H–C contacts as H bonds if $\textit{r}(\text{OC}) \leq 3.2 \text{ Å}$ and $\angle\,\text{OHC} \geq 90^\circ$. The optimized structures were also used to predict collision cross-section CCS calc through N_2 at 300 K. We implemented the trajectory method within the IMoS program, wherein a Verlet algorithm computes a Lennard-Jones 4-6-12 potential for the ion and N_2 species. 49

SUPPLEMENTAL INFORMATION

Supplemental information can be found online at https://doi.org/10.1016/j.xcrp. 2024.102071.

ACKNOWLEDGMENTS

This work was funded by a National Science Foundation CheMIE REU award (2150510) and Texas State University. The UK HEC Materials Chemistry Consortium, funded by EPSRC (EP/R029431 and EP/X035859/1), enabled use of the ARCHER2 UK National Supercomputing Service.

AUTHOR CONTRIBUTIONS

D.S. designed research; D.S. and R.R.R. conducted the experiments and interpreted data; U.T. performed theoretical calculations; D.S. wrote the paper.

DECLARATION OF INTERESTS

The authors declare no competing interests.

Received: March 25, 2024 Revised: June 5, 2024 Accepted: June 7, 2024 Published: June 28, 2024

REFERENCES

- Arias-Rotondo, D.M., and McCusker, J.K. (2016). The photophysics of photoredox catalysis: a roadmap for catalyst design. Chem. Soc. Rev. 45, 5803–5820. https://doi.org/10. 1039/C6CS00526H
- Tinker, L.L., McDaniel, N.D., and Bernhard, S. (2009). Progress towards solar-powered homogeneous water photolysis. J. Mater. Chem. 19, 3328. https://doi.org/10.1039/ b818112h.
- 3. McCusker, J.K. (2019). Electronic structure in the transition metal block and its implications for light harvesting. Science 363, 484–488. https://doi.org/10.1126/science.aav9104.
- Constable, E.C. (1984). Nucleophilic attack upon coordinated heterocycles; definitive evidence for the enhanced electrophilicity of coordinated pyridines. Inorg. Chim. Acta. 82, 53–57. https://doi.org/10.1016/S0020-1693(00) 82537-2.
- 5. Mulazzani, Q.G., D'Angelantonio, M., Camaioni, N., and Venturi, M. (1991). Reactivity of Ru(bpy)₃⁺ towards the radicals originating from the scavenging of hydrogen atoms and hydroxyl radicals by methanol, ethanol, propan-2-ol, tert-butyl alcohol and formate ions in aqueous solution: a pulse radiolytic

- study. Faraday Trans. 87, 2179. https://doi.org/ 10.1039/ft9918702179.
- Limburg, B., Bouwman, E., and Bonnet, S. (2016). Rate and Stability of Photocatalytic Water Oxidation using [Ru(bpy)₃]²⁺ as Photosensitizer. ACS Catal. 6, 5273–5284. https://doi.org/10.1021/acscatal.6b00107.
- Creutz, C., and Sutin, N. (1975). Reaction of tris(bipyridine)ruthenium(III) with hydroxide and its application in a solar energy storage system. Proc. Natl. Acad. Sci. USA 72, 2858– 2862. https://doi.org/10.1073/pnas.72.8.2858.
- Zelenka, J., and Roithová, J. (2020). Mechanistic Investigation of Photochemical Reactions by Mass Spectrometry. ChemBioChem 21, 2232–2240. https://doi.org/ 10.1002/cbic.202000072.
- Katta, V., Chowdhury, S.K., and Chait, B.T. (1990). Electrospray ionization: a new tool for the analysis of ionic transition-metal complexes. J. Am. Chem. Soc. 112, 5348–5349. https://doi.org/10.1021/ja00169a051.
- Bignozzi, C.A., Bortolini, O., Curcuruto, O., and Hamdan, M. (1994). Investigation of ruthenium(II) and iron(II) tris-bipyridyl complexes by means of 10-30 keV Cs⁺ ion

- bombardment and collision-induced dissociation. Rapid Commun. Mass Spectrom. 8, 706–710. https://doi.org/10.1002/rcm. 1290080909.
- Earley, J.D., Zieleniewska, A., Ripberger, H.H., Shin, N.Y., Lazorski, M.S., Mast, Z.J., Sayre, H.J., McCusker, J.K., Scholes, G.D., Knowles, R.R., et al. (2022). Ion-pair reorganization regulates reactivity in photoredox catalysts. Nat. Chem. 14, 746–753. https://doi.org/10.1038/s41557-022-00911-6
- Wyttenbach, T., Pierson, N.A., Clemmer, D.E., and Bowers, M.T. (2014). Ion Mobility Analysis of Molecular Dynamics. Annu. Rev. Phys. Chem. 65, 175–196. https://doi.org/10.1146/ annurev-physchem-040513-103644.
- Butschke, B., and Schwarz, H. (2012). "Rollover" cyclometalation – early history, recent developments, mechanistic insights and application aspects. Chem. Sci. 3, 308–326. https://doi.org/10.1039/C1SC00651G.
- Stebens, G., and Butschke, B. (2023). Probing Intermediates of lon/Molecule Reactions by their Independent Gas-Phase Synthesis and Fragmentation – The Thiomethoxymethyl Complexes [(bipy)M(CH₂SCH₃)]⁺ (M = Pt, Pd,

Article



- Ni). Isr. J. Chem. 63, e202300045. https://doi.org/10.1002/ijch.202300045.
- Constable, E.C., and Seddon, K.R. (1982). A deuterium exchange reaction of the tris-(2,2'-bipyridine)ruthenium(II) cation: evidence for the acidity of the 3,3'-protons. J. Chem. Soc., Chem. Commun. 34–36. https://doi.org/ 10.1039/C39820000034.
- O'Hair, R.A.J. (2021). Organometallic gasphase ion chemistry and catalysis: insights into the use of metal catalysts to promote selectivity in the reactions of carboxylic acids and their derivatives. Mass Spectrom. Rev. 40, 782–810. https://doi.org/10.1002/mas.21654.
- Woolley, M., Khairallah, G.N., da Silva, G., Donnelly, P.S., and O'Hair, R.A.J. (2014). Direct versus Water-Mediated Protodecarboxylation of Acetic Acid Catalyzed by Group 10 Carboxylates, [(phen)M(O₂CCH₃)]⁺. Organometallics 33, 5185–5197. https://doi. org/10.1021/om500493w.
- 18. Zavras, A., Khairallah, G.N., Krstić, M., Girod, M., Daly, S., Antoine, R., Maitre, P., Mulder, R.J., Alexander, S.-A., Bonačić-Koutecký, V., et al. (2016). Ligand-induced substrate steering and reshaping of [Ag₂(H)]⁺ scaffold for selective CO₂ extrusion from formic acid. Nat. Commun. 7, 11746. https://doi.org/10.1038/ncomms11746.
- Muñoz-García, A.B., Benesperi, I., Boschloo, G., Concepcion, J.J., Delcamp, J.H., Gibson, E.A., Meyer, G.J., Pavone, M., Pettersson, H., Hagfeldt, A., and Freitag, M. (2021). Dyesensitized solar cells strike back. Chem. Soc. Rev. 50, 12450–12550. https://doi.org/10.1039/ DOCS01336F.
- Boschloo, G., and Hagfeldt, A. (2009). Characteristics of the lodide/Triiodide Redox Mediator in Dye-Sensitized Solar Cells. Acc. Chem. Res. 42, 1819–1826. https://doi.org/10. 1021/ar900138m.
- McIndoe, J.S., and Vikse, K.L. (2019). Assigning the ESI mass spectra of organometallic and coordination compounds. J. Mass Spectrom. 54, 466–479. https://doi.org/10.1002/jms.4359.
- Shen, J., and Brodbelt, J. (1999). Dissociation of doubly charged transition metal/polyether/ pyridyl ligand complexes in a quadrupole ion trap mass spectrometer. J. Am. Soc. Mass Spectrom. 10, 126–135. https://doi.org/10. 1016/\$1044-0305(98)00137-8.
- Herschbach, D.R. (1965). Molecular Beam Studies of Internal Excitation of Reaction Products. Appl. Opt. 4, 128. https://doi.org/10. 1364/AO.4.S1.000128.
- Magee, J.L. (1940). The Mechanism of Reactions Involving Excited Electronic States The Gaseous Reactions of the Alkali Metals and Halogens. J. Chem. Phys. 8, 687–698. https:// doi.org/10.1063/1.1750739.
- Polanyi, J.C., and Woodall, K.B. (1972). Energy Distribution Among Reaction Products. VI. F+H₂, D₂. J. Chem. Phys. 57, 1574–1586. https://doi.org/10.1063/1.1678438.
- Calzadiaz-Ramirez, L., and Meyer, A.S. (2022). Formate dehydrogenases for CO₂ utilization. Curr. Opin. Biotechnol. 73, 95–100. https://doi. org/10.1016/j.copbio.2021.07.011.

- Riddlestone, I.M., Kraft, A., Schaefer, J., and Krossing, I. (2018). Taming the Cationic Beast: Novel Developments in the Synthesis and Application of Weakly Coordinating Anions. Angew. Chem. Int. Ed. 57, 13982–14024. https://doi.org/10.1002/anie.201710782.
- Peltzer, R.M., Gauss, J., Eisenstein, O., and Cascella, M. (2020). The Grignard Reaction – Unraveling a Chemical Puzzle. J. Am. Chem. Soc. 142, 2984–2994. https://doi.org/10.1021/ jacs.9b11829.
- Hunter E.P., Lias S.G. Mass Spectrometry: Proton Affinities, Encyclopedia of Spectroscopy and Spectrometry. In: Linstrom P. J., Mallard W. G., editors. NIST Chemistry WebBook, NIST Standard Reference Database Number 69. National Institute of Standards and Technology. https://doi.org/10.18434/T4D303.
- Peláez, R.J., Blondel, C., Delsart, C., and Drag, C. (2009). Pulsed photodetachment microscopy and the electron affinity of iodine. J. Phys. B: At. Mol. Opt. Phys. 42, 125001. https://doi.org/10.1088/0953-4075/42/12/ 125001
- Blondel, C., Cacciani, P., Delsart, C., and Trainham, R. (1989). High-resolution determination of the electron affinity of fluorine and bromine using crossed ion and laser beams. Phys. Rev. A 40, 3698–3701. https://doi. org/10.1103/PhysRevA.40.3698.
- Berzinsh, U., Gustafsson, M., Hanstorp, D., Klinkmüller, A., Ljungblad, U., and Mårtensson-Pendrill, A. (1995). Isotope shift in the electron affinity of chlorine. Phys. Rev. A 51, 231–238. https://doi.org/10.1103/PhysRevA.51.231.
- Rillema, D.P., Allen, G., Meyer, T.J., and Conrad, D. (1983). Redox properties of ruthenium(II) tris chelate complexes containing the ligands 2,2'-bipyrazine, 2,2'-bipyridine, and 2,2'-bipyrimidine. Inorg. Chem. 22, 1617–1622. https://doi.org/10.1021/ic00153a012.
- Barigelletti, F., Juris, A., Balzani, V., Belser, P., and Von Zelewsky, A. (1987). Influence of the ligand structure on the electrochemical and spectroscopic properties of ruthenium(II)polypyridine complexes. Inorg. Chem. 26, 4115–4119. https://doi.org/10.1021/ ic00271a029
- Byskov, C.S., Weber, J.M., and Nielsen, S.B. (2015). Gas-phase spectroscopy of singly reduced tris(bipyridine)ruthenium ions, Ru(bipy)₃⁺. Phys. Chem. Chem. Phys. 17, 5561– 5564. https://doi.org/10.1039/C4CP05477F.
- Munshi, M.U., Martens, J., Berden, G., and Oomens, J. (2020). Vibrational Spectra of the Ruthenium—Tris-Bipyridine Dication and Its Reduced Form in Vacuo. J. Phys. Chem. A 124, 2449–2459. https://doi.org/10.1021/acs.jpca. 0c00888.
- Scarborough, C.C., Sproules, S., Weyhermüller, T., DeBeer, S., and Wieghardt, K. (2011). Electronic and Molecular Structures of the Members of the Electron Transfer Series [Cr(tbpy)₃]ⁿ (n = 3+, 2+, 1+, 0): An X-ray Absorption Spectroscopic and Density Functional Theoretical Study. Inorg. Chem. 50, 12446–12462. https://doi.org/10.1021/ ic/2011/23x.

- Ruotolo, B.T., Benesch, J.L.P., Sandercock, A.M., Hyung, S.-J., and Robinson, C.V. (2008). Ion mobility-mass spectrometry analysis of large protein complexes. Nat. Protoc. 3, 1139– 1152. https://doi.org/10.1038/nprot.2008.78.
- Collette, C., and De Pauw, E. (1998). Calibration of the internal energy distribution of ions produced by electrospray. Rapid Commun. Mass Spectrom. 12, 165–170. https://doi.org/10.1002/(SICI)1097-0231(19980227) 12:4<165::AID-RCM140>3.0.CO;2-1.
- Broomhead, J.A., Young, C.G., and Hood, P. (2007). Tris(2,2'-Bipyridine)Ruthenium(II) Dichloride Hexahydrate. Inorg. Synth. 28, 338–340. https://doi.org/10.1002/9780470132593.ch86.
- Elgar, C.E., Yusoh, N.A., Tiley, P.R., Kolozsvári, N., Bennett, L.G., Gamble, A., Péan, E.V., Davies, M.L., Staples, C.J., Ahmad, H., and Gill, M.R. (2023). Ruthenium(II) Polypyridyl Complexes as FRET Donors: Structure- and Sequence-Selective DNA-Binding and Anticancer Properties. J. Am. Chem. Soc. 145, 1236–1246. https://doi.org/10.1021/jacs. 2c11111.
- Lenhart, D., Bauer, A., Pöthig, A., and Bach, T. (2016). Enantioselective Visible-Light-Induced Radical-Addition Reactions to 3-Alkylidene Indolin-2-ones. Chem. Eur J. 22, 6519–6523. https://doi.org/10.1002/chem.201600600.
- Kühne, T.D., Iannuzzi, M., Del Ben, M., Rybkin, V.V., Seewald, P., Stein, F., Laino, T., Khaliullin, R.Z., Schütt, O., Schiffmann, F., et al. (2020).
 CP2K: An electronic structure and molecular dynamics software package - Quickstep: Efficient and accurate electronic structure calculations. J. Chem. Phys. 152, 194103. https://doi.org/10.1063/5.0007045.
- Goedecker, S., Teter, M., and Hutter, J. (1996). Separable dual-space Gaussian pseudopotentials. Phys. Rev. B 54, 1703–1710. https://doi.org/10.1103/PhysRevB.54.1703.
- Perdew, J.P., Burke, K., and Ernzerhof, M. (1996). Generalized Gradient Approximation Made Simple. Phys. Rev. Lett. 77, 3865–3868. https://doi.org/10.1103/PhysRevLett.77.3865.
- VandeVondele, J., and Hutter, J. (2007). Gaussian basis sets for accurate calculations on molecular systems in gas and condensed phases. J. Chem. Phys. 127, 114105. https:// doi.org/10.1063/1.2770708.
- Byrd, R.H., Lu, P., Nocedal, J., and Zhu, C. (1995). A Limited Memory Algorithm for Bound Constrained Optimization. SIAM J. Sci. Comput. 16, 1190–1208. https://doi.org/10. 1137/0916069.
- Nosé, S. (1984). A unified formulation of the constant temperature molecular dynamics methods. J. Chem. Phys. 81, 511–519. https:// doi.org/10.1063/1.447334.
- 49. Coots, J., Gandhi, V., Onakoya, T., Chen, X., and Larriba-Andaluz, C. (2020). A parallelized tool to calculate the electrical mobility of charged aerosol nanoparticles and ions in the gas phase. J. Aerosol Sci. 147, 105570. https://doi.org/10.1016/j.jaerosci.2020.105570.